Calculation of the magnetic flux density distribution in type-II superconductors with finite thickness and well-defined geometry

A. Forkl and H. Kronmüller
Max-Planck-Institut für Metallforschung, Institut für Physik, D-70506 Stuttgart, Germany
(Received 3 May 1995)

The distribution of the critical current density $\mathbf{j}_c(\mathbf{r})$ in hard type-II superconductors depends strongly on their sample geometry. Rules are given for the construction of $\mathbf{j}_c(\mathbf{r})$. Samples with homogeneous thickness are divided into cakelike regions with a unique current direction. The spatial magnetic flux density distribution and the magnetic polarization of such a cakelike unit cell with homogeneous current density are calculated analytically. The magnetic polarization and magnetic flux density distribution of a superconductor in the mixed state is then given by an adequate superposition of the unit cell solutions. The theoretical results show good agreement with magneto-optically determined magnetic flux density distributions of a quadratic thin superconducting $YBa_2Cu_3O_{7-x}$ film. The current density distribution is discussed for several sample geometries.

I. INTRODUCTION

After the cooling of a type-II superconductor in zero magnetic field from $T>T_c$ to $T<T_c$ and application of external magnetic fields $\mu_0 H_{\text{ext}}$, the penetration of magnetic flux into the sample takes place in several steps.

(I) Meissner phase ($\mu_0 H_{\text{ext}}<\mu_0 H_{c1}$): Meissner surface currents $\mathbf{j}_M(\mathbf{r})$, flowing in a depth λ, prevent the penetration of magnetic flux into the sample. The magnetic flux density $\mathbf{B}_i$ inside of the sample is zero.

(II) Partly penetrated Shubnikov phase ($\mu_0 H_{c1}<\mu_0 H_{\text{ext}}<\mu_0 H^*$): Quantized magnetic flux enters the sample. Due to pinning forces, acting on the flux lines, the quantized flux cannot fill up the sample homogeneously. Accordingly, a flux front builds up, penetrating into the sample up to a certain penetration depth determined by the applied field. With increasing external magnetic field, the flux front penetrates deeper into the sample. The inhomogeneous distribution of magnetic flux causes a critical current density $\mathbf{j}_c(\mathbf{r})$, producing a Lorentz force acting on the flux lines. The Lorentz force is balanced by the pinning forces. The critical current density causes a magnetic stray field in the flux-free region. This stray field will be compensated by the stray field of additional inner shielding currents $\mathbf{j}_s(\mathbf{r})$. The critical current density $\mathbf{j}_c(\mathbf{r})$ flows only in the region where magnetic flux has penetrated, whereas the inner shielding currents $\mathbf{j}_s(\mathbf{r})$ flow in the surface region of the flux-free zone. For thin samples, $\mathbf{j}_s(\mathbf{r})$ flows in the whole flux-free zone.

(III) Fully penetrated Shubnikov phase ($\mu_0 H^*<\mu_0 H_{\text{ext}}<\mu_0 H_{c2}$): At $\mu_0 H_{\text{ext}}=\mu_0 H^*$ the flux front has reached the sample center. Now in the whole sample the critical current density flows. With increasing external magnetic field, the sample fills up further with magnetic flux. Caused by the increase of the local magnetic flux density, the pinning forces and therefore the local critical current density change.

(IV) Normal conducting state ($\mu_0 H_{\text{ext}}>\mu_0 H_{c2}$): At $\mu_0 H_{\text{ext}}=\mu_0 H_{c2}$ the currents have decreased to zero, and in the field range $\mu_0 H_{\text{ext}}>\mu_0 H_{c2}$ the sample behaves as in the normal conducting state. Only the fluxon is quantized, and some quantization remains until $\mu_0 H_{c3}=1.7\,\mu_0 H_{c2}$.

The electric current density distribution $\mathbf{j}(\mathbf{r})$ flowing in the volume V of the superconductor in steps I–III produces a macroscopic magnetic polarization $\mu_0\mathbf{M}$ given by

$$\mu_0\mathbf{M}=\frac{\mu_0}{2V}\int_V \mathbf{r}\times\mathbf{j}(\mathbf{r})\,d^3r \tag{1}$$

and a magnetic self-field $\mu_0\mathbf{H}_{\text{self}}(\mathbf{r})$, which can be calculated from the Biot-Savart law

$$\mu_0\mathbf{H}_{\text{self}}(\mathbf{r})=\frac{\mu_0}{4\pi}\int_V \frac{\mathbf{j}(\mathbf{r}')\times(\mathbf{r}-\mathbf{r}')}{|\mathbf{r}-\mathbf{r}'|^3}\,d^3r'. \tag{2}$$

The local magnetic flux density $\mathbf{B}(\mathbf{r})$ is then a superposition of the self-field $\mu_0\mathbf{H}_{\text{self}}(\mathbf{r})$ of the sample and the external magnetic field $\mu_0\mathbf{H}_{\text{ext}}$,

$$\mathbf{B}(\mathbf{r})=\mu_0\mathbf{H}_{\text{self}}(\mathbf{r})+\mu_0\mathbf{H}_{\text{ext}}. \tag{3}$$

Within the Bean model, as first introduced by Bean,[1] the absolute value $|\mathbf{j}_c(\mathbf{r})|$ of the critical current density is spatially constant, but the direction of $\mathbf{j}_c(\mathbf{r})$ depends strongly on the sample geometry. Under the assumption of such a field-independent critical current density and by neglecting the Meissner surface currents $\mathbf{j}_M(\mathbf{r})$, the magnetic polarization and the magnetic flux density distribution can be calculated for special geometries of the sample.

For partially penetrated magnetic flux and in the one-dimensional cases of thin strips and circular disks of thickness much less than the lateral extension, Brandt *et al.*[2] and Mikheenko and Kuzovlev[3] calculated the inner shielding currents $\mathbf{j}_s$ required to keep the central zone flux free. The analytical solutions for the magnetic flux density distribution and magnetic polarization depend on the penetration depth of the flux front. For thin rectangular samples, an analytical $\mathbf{B}(\mathbf{r})$ solution was found recently for the fully penetrated state.[4] For partially penetrated flux, only numerical results exist.[5] The numerical solutions based on time integration of a

0163-1829/95/52(22)/16130(10)/$06.00

nonlocal (due to the transverse geometry) and nonlinear (due to the strongly nonlinear current-voltage curve of superconductors) diffusion equation have the advantage that any $j_c(B)$ dependence may be assumed. These points are discussed in some detail in the comprehensive and excellent review paper of Brandt.[5] Besides these "first-principles calculations" of J and H, mathematical algorithms were developed to calculate $j(r)$ from experimental $B(r)$ data[6,7] by inverting Ampère's law.

For samples with finite thickness, there exists an analytical $\mathbf{B}(\mathbf{r})$ solution only for strips in the fully penetrated state.[8] The results show that for samples with a ratio thickness D to width W smaller than about 0.2 the flux density profiles are curved and the calculation of j_c from experimental data requires a detailed analysis as performed in Ref. 9. Also, the calculation of j_c from magnetization measurements has to take into account the real shape of the sample.[10,11] The present paper is a further contribution towards this goal.

Using the Bean model, i.e., $|\mathbf{j}_c(\mathbf{r})|=\text{const}$, this paper describes the distribution of the direction of $\mathbf{j}_c(\mathbf{r})$ in samples with homogeneous finite thickness and for well-defined geometry. Further on, it is shown how to get analytical $\mathbf{B}(\mathbf{r})$ distributions in the fully penetrated state, for example, in a quadratic sample with anisotropic critical current density. The calculations are compared with $\mathbf{B}(\mathbf{r})$ distributions measured by the magneto-optical Faraday effect, and good agreement is obtained.

II. EXPERIMENTAL BACKGROUND AND RESULTS

The magneto-optical Faraday effect serves as an excellent tool for the visualization of the magnetic flux density on the surface of superconductors. For the application of this technique, a first reflective layer, e.g., Al, and a second magneto-optical layer, composed of a mixture of EuS diluted by EuF_2, is evaporated onto the sample. The EuS/EuF_2 layer shows a high Verdet's constant at temperatures $T<17$ K. Therefore the polarization of a linearly polarized light beam, passing through the magneto-optical layer, will be rotated by an angle which is proportional to the local magnetic flux density $B_\parallel$ parallel to the beam direction. Regions with different magnetic flux densities are seen through an analyzer with different light intensities, i.e., dark and bright areas. The Al layer increases the surface reflectivity and therefore the contrast. Usually, the light beam is perpendicular to the sample surface. Therefore the calibration of light intensities yields the B_z component of the magnetic flux density in the surface of the superconductor. Using an air coil, magnetic fields up to 400 mT can be applied. For details, see Ref. 12.

c-axis-oriented $YBa_2Cu_3O_{7-x}$-films with a thickness of 300 nm were evaporated onto $SrTiO_3$ substrates by laser ablation.[13] Then quadratic samples with a 2-mm edge length were patterned by standard lithographic techniques. After evaporation of Al (thickness $d_{Al}=200$ nm) and EuS/EuF_2 (thickness $d_{Eu}=250$ nm), the samples were cooled in zero magnetic field from room temperature to helium temperature. For this, a cryostat was used which is designed for light microscopical investigations. In external applied magnetic fields, the occurrence of magnetic flux is seen as an increase of the light intensity. These changes are detected by a low-light-level video camera, which is connected to a digital image-processing system for quantitative analysis. The observed flux patterns are represented in Figs. 1(a)–1(f) for different applied magnetic fields. Bright areas belong to regions with penetrated magnetic flux.

At $\mu_0 H_{ext}=26.5$ mT magnetic flux has penetrated partly into the film, building up a flux front. The inner part of the sample and the corners are flux free, whereas in the middle of the edges the flux could penetrate deeper [Fig. 1(a)]. Caused by some inhomogeneities in the film morphology, the flux front itself is not homogeneous. At the boarder some irregularities rise to a funnel-like flux pattern. With increasing $\mu_0 H_{ext}$ the flux penetrates deeper into the sample [Figs. 1(b) and 1(c)]. The diagonals still stay flux free up to $\mu_0 H_{ext}\approx 110$ mT as indicated by a dark cross pattern. With further increase of $\mu_0 H_{ext}$, the diagonals also fill up with magnetic flux, and at $\mu_0 H_{ext}=155.5$ mT, only a small part in the middle of the sample is flux free [Fig. 1(e)]. In the remanent state after reducing the external field to zero [Fig. 1(f)], the flux is kept in the sample by the pinning forces. The dark region in the center of the sample indicates that there no flux had penetrated at $\mu_0 H_{ext}=155.5$ mT. The field H^* necessary for full flux penetration is reached when in the remanent state no dark region in the center is visible. This is the case at $\mu_0 H_{ext}=263.2$ mT. For fields $H_{ext}>H^*$ the flux pattern does not change and the local flux density increases with increasing $\mu_0 H_{ext}$.

In Figs. 2(a)–2(f) the flux penetration is shown for a triangular patterned film. Here also magnetic flux starts to penetrate at the middle of the edges, whereas the corners rest flux free up to a certain external field. This result was also obtained in Ref. 14. In the remanent state the bisectors are full with flux. This is also observed in the remanent state of other sample geometries,[15–17] for example, in rectangular structured films [Figs. 3(a)–3(f)].

From the above observations and from the knowledge about the current density distributions in circular-shaped and strip-structured films,[8,12] a current model, as shown in Fig. 4, can be derived for the fully penetrated state of a quadratic sample with isotropic current density. The critical current density $\mathbf{j}_c(\mathbf{r})$ flows in the whole sample and parallel to the nearest edge. This requires that the currents change direction by crossing the diagonals. Therefore the sample can be divided into four isosceles triangles, each with a homogeneous current density parallel to the base line. To prove the validity of this model, the self-field of the current density distribution has to be calculated and compared with the experimentally determined B_z distribution.

III. CALCULATION OF MAGNETIC FLUX DENSITY DISTRIBUTION

The central idea of this paper is the analytical calculation of the magnetic flux density distribution $\mathbf{B}(\mathbf{r})$ of a homogeneous current density distribution $\mathbf{j}(\mathbf{r})$ flowing in a cakelike region $\mathscr{R}$ as shown in Fig. 5(a). This basic "brick" may then be used to calculate more complicated specimen shapes by linear superposition. In a Cartesian x,y,z-coordinate system, the current density distribution is then given by

$$\mathbf{j}(\mathbf{r})=(j_c,0,0), \tag{4}$$

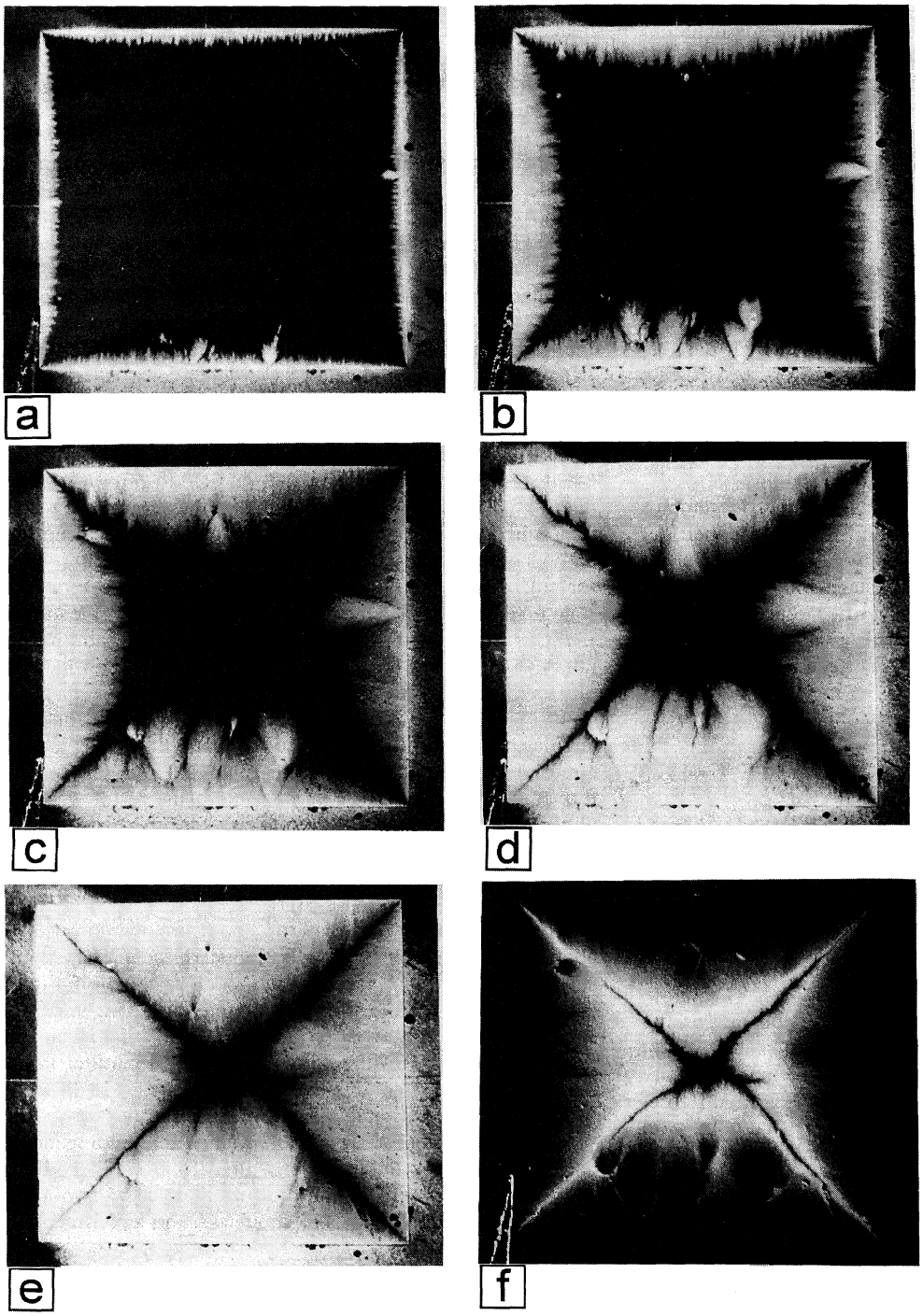

FIG. 1. Magnetic flux distribution pattern of a 300-nm-thick square-shaped $YBa_2Cu_3O_{7-x}$ film after zero-field cooling and application of external magnetic fields $\mu_0 H_{ext}$ of (a) 26.5 mT, (b) 44.3 mT, (c) 73.2 mT, (d) 100.3 mT, (e) 155.5 mT perpendicular to the film and (f) in the remanent state.

flowing in the region

$$\mathcal{R}=\begin{cases} k_1 y \leq x \leq k_2 y, \\ R_1 \leq y \leq R_2, \\ -D/2 \leq z \leq +D/2. \end{cases} \tag{5}$$

The parameters k_1 and k_2 are related to the angles δ_1 and δ_2 of Fig. 5(a) by $\delta_{1,2}=\text{arccot}|k_{1,2}|$. D is the thickness and R_2-R_1 the depth of the cake. The volume is given by $V=(D/2)(R_2^2-R_1^2)(|k_1|+|k_2|)$.

The Biot-Savart law yields the magnetic flux density distribution

$$\mathbf{B}(\mathbf{r})=(0,B_y(x,y,z),B_z(x,y,z)), \tag{6}$$

where

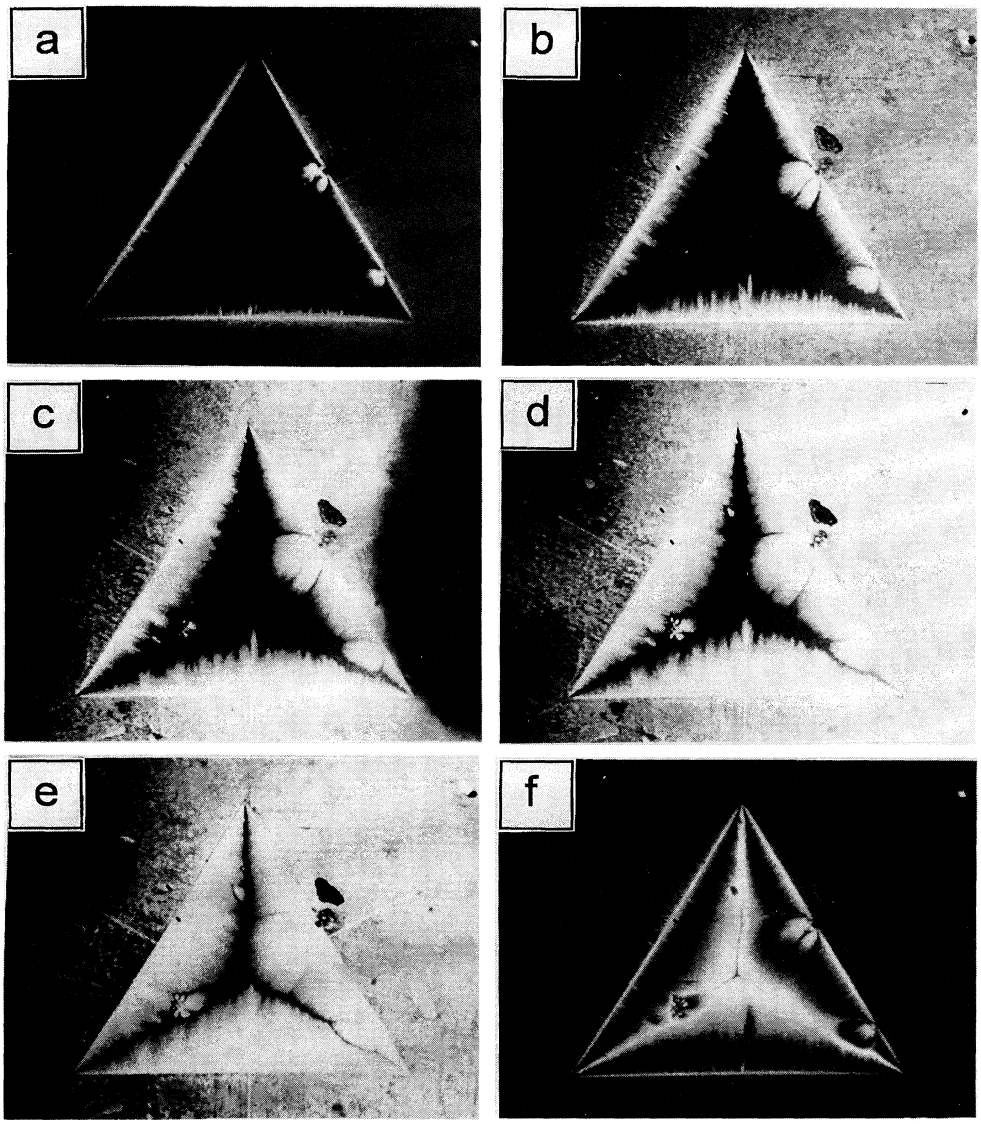

FIG. 2. Magnetic flux distribution pattern of a 300-nm-thick triangular-shaped $YBa_2Cu_3O_{7-x}$ film after zero-field cooling and application of external magnetic fields $\mu_0 H_{ext}$ of (a) 19.5 mT, (b) 38.0 mT, (c) 56.3 mT, (d) 75.4 mT, (e) 135.3 mT perpendicular to the film and (f) in the remanent state after application of a maximum external field of 222.3 mT.

$$B_{y,z}=\frac{\mu_0 j_c}{4\pi}\{K_{y,z}(\alpha_1,\eta_1,\zeta_1)+K_{y,z}(\alpha_2,\eta_1,\zeta_1)-K_{y,z}(\alpha_1,\eta_1,\zeta_2)-K_{y,z}(\alpha_2,\eta_1,\zeta_2)-K_{y,z}(\alpha_1,\eta_2,\zeta_1)-K_{y,z}(\alpha_2,\eta_2,\zeta_1)+K_{y,z}(\alpha_1,\eta_2,\zeta_2)+K_{y,z}(\alpha_2,\eta_2,\zeta_2)\}, \tag{7}$$

with the abbreviations $\alpha_{1,2}=-x/k_{1,2}-y$, $\eta_{1,2}=y-R_{1,2}$, and $\zeta_{1,2}=z\pm D/2$. The functions K_y and K_z are given by

$$K_y(\alpha,\eta,\zeta)=\sum_{\nu=\pm 1}\left\{\zeta\ \arctan\left[\frac{\eta\tau+\sqrt{\sigma^2+\zeta^2}-\nu\alpha k}{\zeta(k+\nu\tau)}\right]+\frac{\nu\eta}{2}\ \ln\left[\varphi^2+\sigma^2-2k\varphi\nu(\alpha+\eta)\right]\right\}+\frac{\alpha k}{\tau}\ \ln\left[\frac{\sigma\varphi\tau}{\tau(\varphi^2+\sigma^2)+2\varphi(\eta+k^2(\alpha+\eta))}\right], \tag{8}$$

$$K_z(\alpha,\eta,\zeta)=\eta\ \arctan\left[\frac{k\zeta(\alpha+\eta)}{\eta\sqrt{\sigma^2+\zeta^2}}\right]+\frac{k\zeta}{\tau}\ \ln\frac{\psi}{\xi}+\sum_{\nu=\pm 1}\left\{\frac{\zeta\alpha k^2}{|\zeta|\tau^2}\ \arctan\left[\frac{\nu\psi+|\zeta|\tau}{\alpha k}\right]+\frac{\nu\alpha k\zeta}{2\tau^2|\zeta|}\ \ln\left[\psi^2+\xi^2-2\nu|\zeta|\psi\tau\right]+\frac{\nu|\alpha|\zeta}{2\alpha}\ \ln\left[\alpha^2\psi(\psi-2k\lambda)+\xi^2\lambda^2\right]\right\}, \tag{9}$$

where the abbreviations $\psi=\eta\tau^2+\alpha k^2+\sqrt{\xi^2+(\eta\tau^2+\alpha k^2)}$, $\xi=\sqrt{\alpha^2k^2+\zeta^2\tau^2}$, $\lambda=\alpha k+|\alpha|\nu\tau$, $\sigma=\sqrt{\eta^2+k^2(\alpha+\eta)^2}$, $\varphi=\zeta+\sqrt{\sigma^2+\zeta^2}$, and $\tau=\sqrt{1+k^2}$ have been used.

By means of Eqs. (7)–(9), it is possible to determine the self-field $\mathbf{B}_{self}(\mathbf{r})$ of a type-II superconductor in the fully pen-

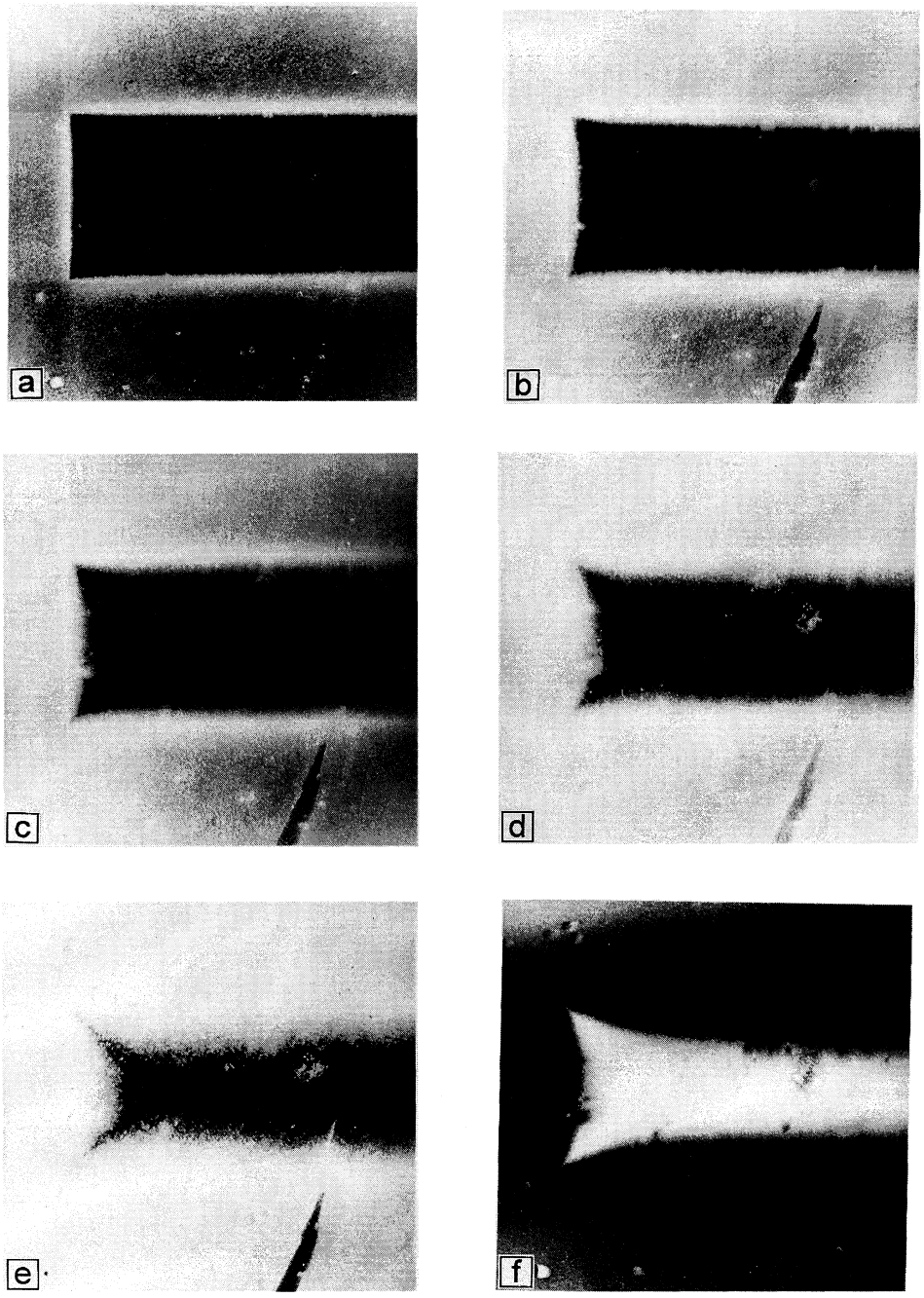

FIG. 3. Magnetic flux distribution pattern of a 300-nm-thick rectangular-shaped $YBa_2Cu_3O_{7-x}$ film after zero-field cooling and application of external magnetic fields $\mu_0 H_{ext}$ of (a) 32.9 mT, (b) 65.8 mT, (c) 98.7 mT, (d) 131.6 mT, (e) 197.4 mT perpendicular to the film and (f) in the remanent state after application of a maximum external field of 263.5 mT.

etrated state. The sample has to be divided into N cake-shaped regions $\mathscr{R}_i$ $(i=1,2,\ldots,N)$ with homogeneous current yielding a self-field $\mathbf{B}_{i,\mathrm{self}}(\mathbf{r})$ according Eqs. (7)–(9). $\mathbf{B}_{\mathrm{self}}(\mathbf{r})$ is then given by the superposition of all $\mathbf{B}_{i,\mathrm{self}}(\mathbf{r})$, i.e.,

$$\mathbf{B}_{\mathrm{self}}(\mathbf{r})=\sum_{i=1}^{N}\mathbf{B}_{i,\mathrm{self}}(\mathbf{r}). \tag{10}$$

The magnetic polarization of the sample is then given by

$$\mu_0\mathbf{M}=\frac{\Sigma_i V_i \mu_0 \mathbf{M}_i}{\Sigma_i V_i}, \tag{11}$$

where the magnetic polarization $\mu_0\mathbf{M}_i$ of the region $\mathscr{R}_i$ depends on the coordinate system according to Eq. (1). In the general case of Fig. 5(b), $\mu_0\mathbf{M}_i$ is given by

$$\mu_0\mathbf{M}_i=\left(0,0,\frac{\mu_0 j_c D}{2V_i}(\tan\delta_1+\tan\delta_2)\left[(x_0\cos\theta+y_0\sin\theta)\frac{R_2^2-R_1^2}{2}+\frac{R_2^3-R_1^3}{3}\right]\right), \tag{12}$$

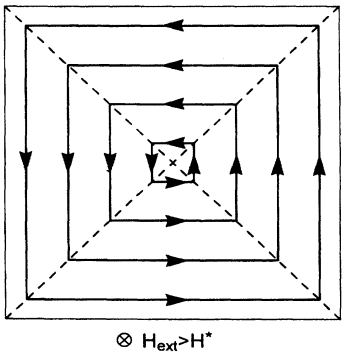

FIG. 4. Model of the current density distribution in a quadratic sample for fully penetrated magnetic flux.

where $V_i=(D/2)(R_2^2-R_1^2)(\tan\delta_1+\tan\delta_2)$ is the volume of the region $\mathscr{R}_i$; i.e., the volume V of the whole sample is given by $V=\Sigma_i V_i$.

IV. DISCUSSION

In the following the current density distribution $\mathbf{j}_c(\mathbf{r})$ in step (III) of flux penetration will be described for four different samples.

(a) Regular polygons with N corners ($N=3,4,5,...$). The sample is divided into isosceles triangles with $R_1=0$ and $-k_1=k_2=\tan(\pi/N)$. The simplest case $N=2$, i.e., $k_{1,2}\rightarrow\mp\infty$, yields the field distribution in a bar, the limit $N\rightarrow\infty$; i.e., $k_{1,2}\rightarrow\mp 0$ yields the distribution in a cylinder. An example for the construction of the current path is shown in Fig. 4 for $N=4$. Figure 6(a) shows the current paths of a triangular sample and, accordingly, Fig. 6(b) the calculated flux distribution in the surface, i.e., the B_z component of the magnetic flux density, which agrees with the experimentally determined density of Fig. 2(e). The calculations were performed with the sample dimensions of Figs. 2(a)–2(f) (thickness $D=300$ nm, edge length 2 mm, height above center, $D/2+d_{Al}+d_{Eu}/2=475$ nm).

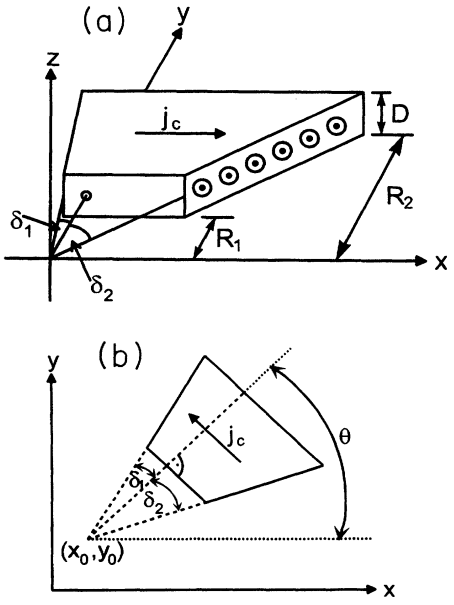

FIG. 5. (a) Cake-shaped region $\mathscr{R}$ with homogeneous current density. The parameters of $\mathscr{R}$ are $R_1, R_2, \delta_1, \delta_2$ and the thickness D. (b) Schematic representation of the used coordinate system for the calculation of $\mu_0\mathbf{M}_i$ [Eq. (12)].

(b) Irregular polygons. An example for the current and magnetic flux density distribution in irregularly shaped samples with straight edges is shown in Figs. 6(c) and 6(d). The current flows always parallel to the nearest edge. Therefore the current path changes direction by crossing the angle bisectors (dashed lines). The regions with homogeneous current direction can always be divided into cakelike regions. Figure 6(e) shows the current paths of a quadratic sample and, accordingly, Fig. 6(f) the flux distribution in the surface, which agrees with the experimentally determined of Fig. 1(e). The calculations were performed with the sample dimensions of Figs. 1(a)–1(f) (thickness $D=300$ nm, edge length 2 mm, height above center, $D/2+d_{Al}+d_{Eu}/2=475$ nm).

(c) Anisotropic current density. The current and magnetic flux density distribution shown in Figs. 6(g) and 6(h) belong to a quadratic sample with anisotropic critical current density. This means that a higher current density j_{ch} flows along one edge direction than j_{cl} in the other edge direction, i.e., $j_{cl}=Aj_{ch}$. The anisotropy factor A of Fig. 6(g) has been chosen to be $A=0.5$. The current paths lie all parallel to the edges and change direction at points which belong to the so-called discontinuity planes. The discontinuity planes separate regions with different current densities $\mathbf{j}_1$ and $\mathbf{j}_2$. For the construction of the discontinuity plane, it has to be taken into account that the current density has no drains and sources, i.e., $\nabla\cdot\mathbf{j}(\mathbf{r})=0$. This yields the general condition

$$\mathbf{j}_1(\mathbf{r})\cdot\mathbf{f}=\mathbf{j}_2(\mathbf{r})\cdot\mathbf{f}, \tag{13}$$

where $\mathbf{f}$ is the normal vector of the discontinuity plane. Therefore the anisotropy factor $A=j_{cl}/j_{ch}$ of Fig. 6(g) is connected to the angle β by $\tan\beta=A$ and to the width b by

$$A=1-b/W. \tag{14}$$

This yields in the isotropic case, i.e., $A=1.0$, $\beta=\pi/4$, and $b=0$ (Fig. 4).

In Figs. 6(f) and 6(h) calculated flux patterns, i.e., the distribution of the B_z component, are presented for a quadratic sample with anisotropy factor A of (a) 1.0 and (b) 0.5. The calculations were performed with the sample dimensions of Figs. 1(a)–1(f) (thickness $D=300$ nm, edge length 2 mm, height above center, $D/2+d_{Al}+d_{Eu}/2=475$ nm). The patterns belong to the case when the flux front has just reached the center. Bright areas represent regions with high flux density, and dark areas, i.e., the diagonals, represent regions where flux could not penetrate easily. This agrees with the experimental observations in Fig. 1(e). The B_z profiles along the diagonal and median of Fig. 6(f), which are represented in Fig. 7, show this strong difference very clear.

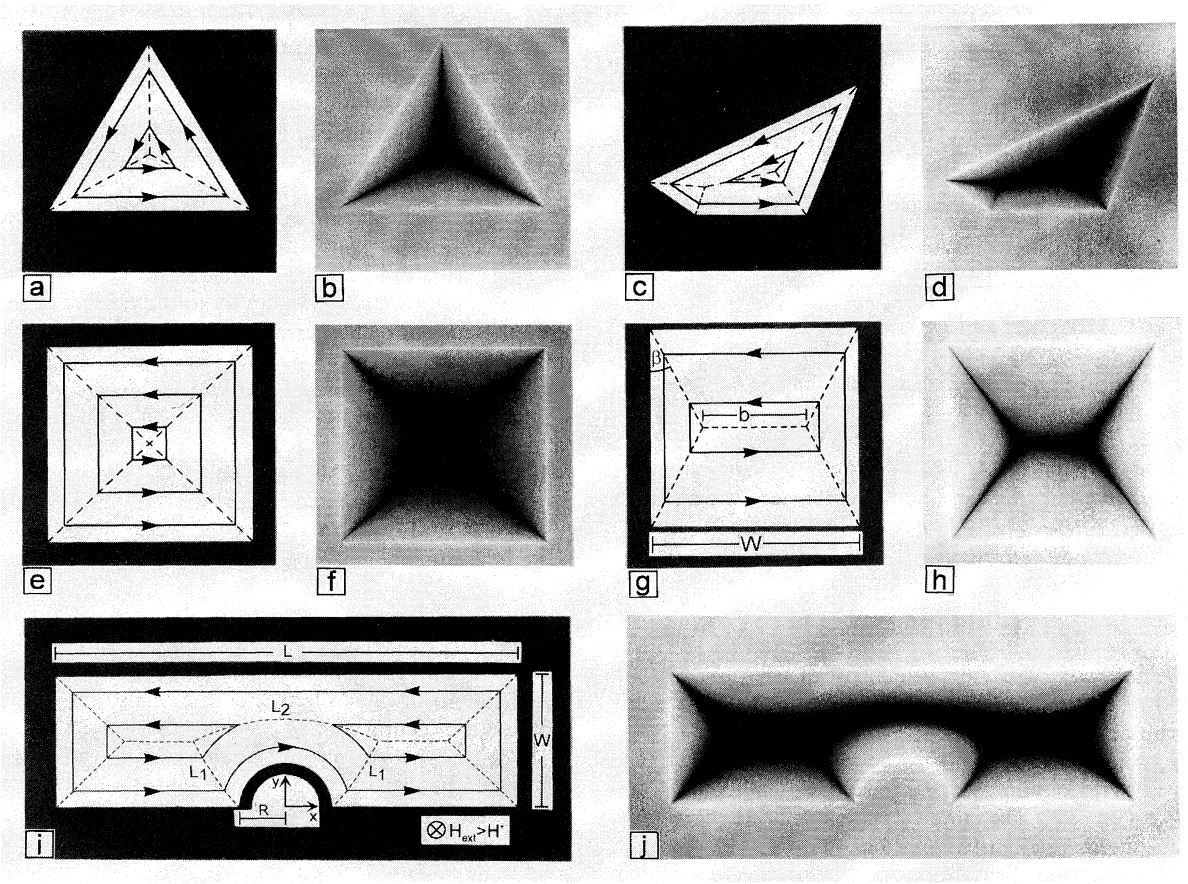

FIG. 6. Current paths and calculated distribution of the B_z component of the magnetic flux density distribution for different sample geometries. Dashed lines belong to the cut of the discontinuity planes with the xy plane; i.e., here the currents change direction. The external magnetic field is always applied perpendicular to the observation plane. (a) and (b) Triangular sample, (c) and (d) irregular polygon-shaped sample, (e) and (f) quadratic sample with anisotropy factor $A=1.0$, (g) and (h) quadratic sample with anisotropic current, i.e., parallel to the horizontal edge flows a lower current $j_{cl}=0.5j_{ch}$ than parallel to the vertical edge (j_{ch}), (i) and (j) rectangular sample with semicircular defect at the edge (radius R). For details see the text.

(d) Samples with curved boundary. The current density distribution shown in Figs. 6(i) and 6(j) belong to an elongated sample (width W, length L) with a semicircular defect (radius R) at the edge and isotropic current density. The current path runs parallel to the edges. That means in a well-defined region $\mathscr{R}_c$ near the defect the current flows on a circular path [Fig. 6(i)].[18]

There exist several discontinuity planes. At the left and right ends of the sample are the same branches as in a quadratic or rectangular sample. Around the defect three further planes exist. From Eq. (13) the discontinuity planes can be calculated. They are all parallel to the z axis and cut the xy plane by curves L_1 and L_2 given by the parabolas $y=(x^2-R^2)/2R$ and $y=[(W+R)^2-x^2]/2(W+R)$, where x and y are defined by the coordinate system of Fig. 6(i).

There are two kinds of current paths depending on their distance to the edge. For distances smaller than $(R-W)/2$, the path goes through the left and right parts of the sample, and for distances between $(R-W)/2$ and $R/2$ the path keeps only in the left or right part [Fig. 6(i)].

The self-field of the circular current in $\mathscr{R}_c$ is given by a sum over M cake like regions with angles $\delta_1=\delta_2=\pi/M$, $R_1=R$, and R_2 according to $L_{1,2}$. This summation does not give the exact self-field of $\mathscr{R}_c$, but is a very good approximation for $M\approx 50$. This is seen from Fig. 8 where the radial distribution of the B_z component in the surface of cylindrical samples is shown for different thicknesses. The profiles are taken by summing up over 100 cakes and show a smooth change.

In Fig. 9 the remanent state of the sample of Figs. 1(a)–1(f) is represented after application of $\mu_0 H_{\text{ext}}=400$ mT. After reducing the external field to zero, the currents and self-field have just changed sign. That means that the flux density profiles of Fig. 9 have to be compared with the calculations of Figs. 6(f) and 6(h) by reversing the light intensities or the associated flux density profiles. In Fig. 9 the discontinuity planes are seen as bright lines where the maximum flux density is kept in the sample.

The funnel-like flux patterns on the right side and on the lower part of Fig. 9 are caused by defects in the morphology

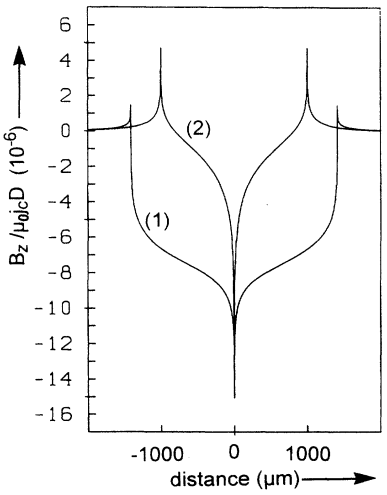

FIG. 7. Calculated B_z component along the diagonal (1) and the median (2) of a quadratic thin film according to Fig. 6(f).

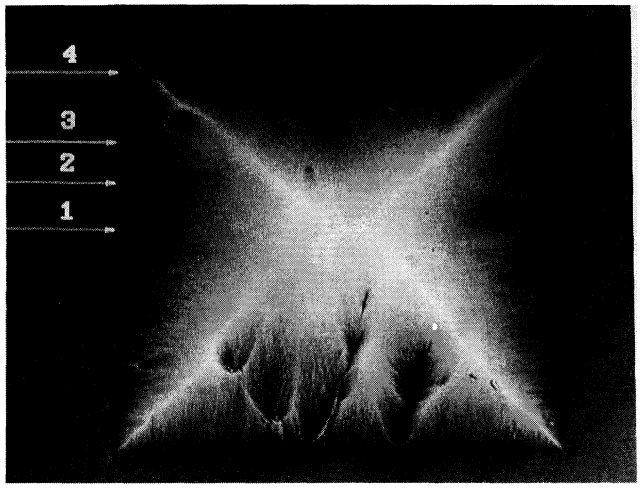

FIG. 9. Remanent magnetic flux distribution pattern of the film shown in Figs. 1(a)–1(f) after application of an external field $\mu_0 H_{ext}$ of 400 mT and reducing to zero.

of the film, giving rise to a current distribution similar to this one in Fig. 6(i). The currents have to go around the defect, and in increasing field the flux can penetrate deeper into the sample compared to regions with smaller defects. Therefore the discontinuity planes do not meet in the geometrical center of the sample. This is also seen in Fig. 9. The discontinuity planes build a small belt of width $b=100$ μm whose center is 58 μm perpendicularly and 48 μm horizontally shifted from the geometrical center. This is a consequence of the obviously higher amount of defects in the lower part than in the upper part of the sample and in the left part than in the right. Two other effects can also generate such a belt: first, a variation of the film thickness. Measurements of the thickness show a change of $\pm 2\%$, which cannot explain the observed great shift. A further explanation is an anisotropy of the critical current as expected by comparing Fig. 9 with Fig. 6(h). According to Eq. (14), the belt width of 100 μm would yield an anisotropy factor A of 0.95. This anisotropy could explain the belt, but not the shift.

Figure 10 shows the measured B_z profiles according to Fig. 9. Along line 1 the width and shift of the bright belt are represented. This profile shows good agreement with the calculated curve (2) of Fig. 7. The maximum B_z values of lines 2 and 3 of Fig. 10 indicate two discontinuity planes. The negative values of B_z in line 4 indicate a negative flux in the remanent state. The wavy shape (wavelength 60–70 μm) of line 4 is caused by macroscopic defects. As mentioned above, the current has to go around the defects and therefore the negative flux can penetrate deeper. Local changes of the film thickness are seen in the measured flux density profiles of Fig. 10 as fluctuations with wavelength of about 5–15 μm.

Circular-shaped samples in general show a homogeneous symmetric flux pattern around the center.[12] If the morphology is disturbed, also a flux belt near the middle of the sample exists. Such a flux distribution is shown in Figs. 11(a)–11(f) for different applied fields. Scratches on the left and right sides of the sample reduce the thickness, leading to

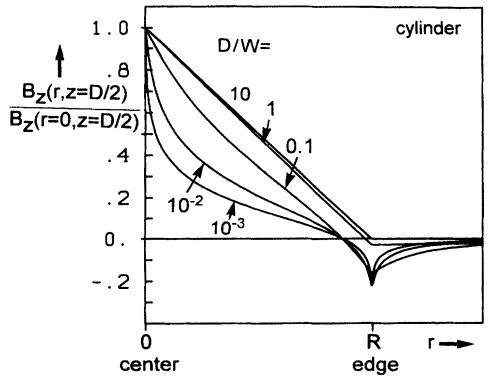

FIG. 8. Calculated radial distribution of the B_z component in the surface of cylinders for different ratios of thickness to radius.

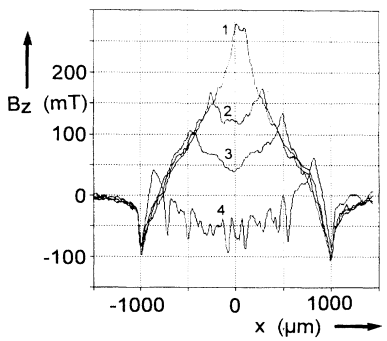

FIG. 10. Representation of the measured B_z profiles according to Fig. 9.

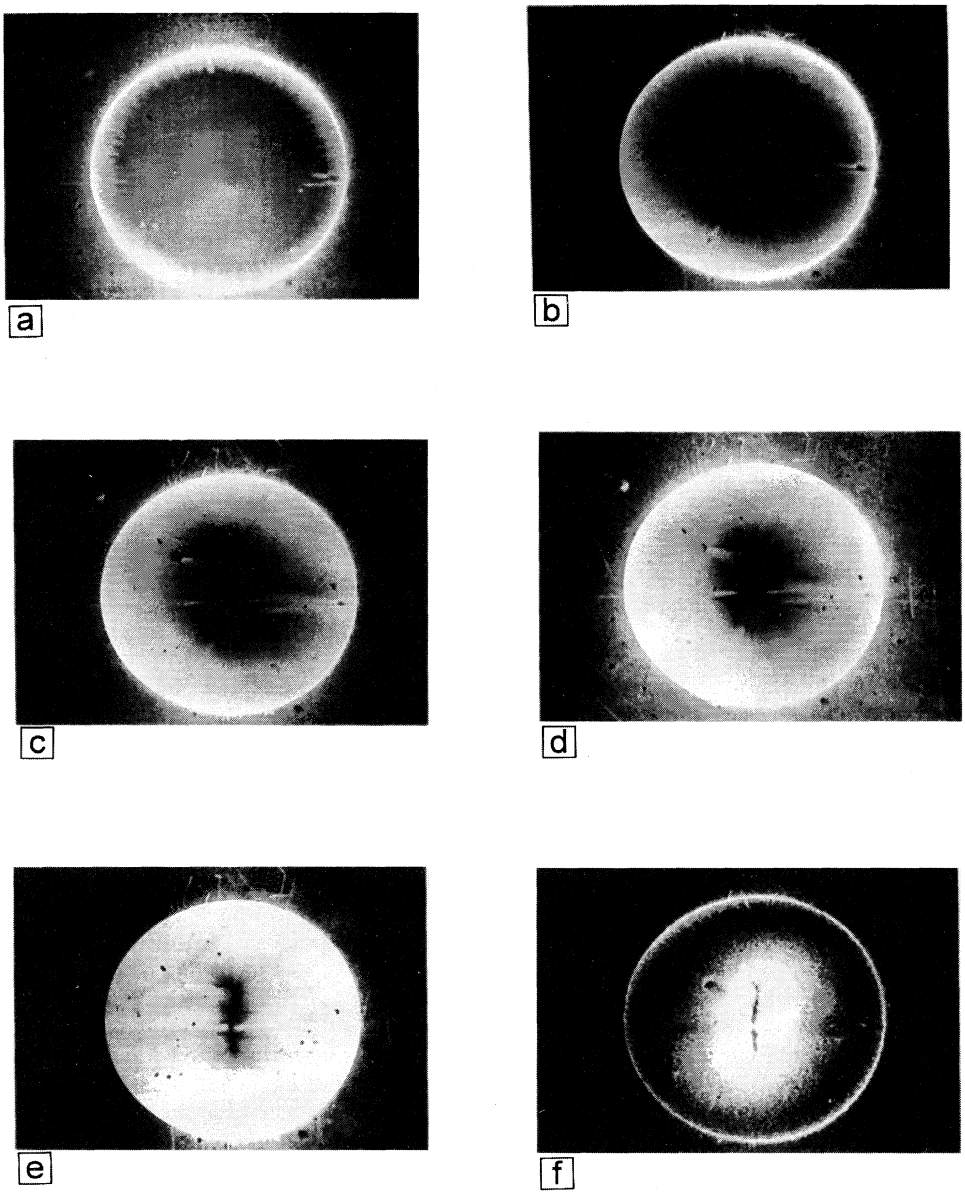

FIG. 11. Magnetic flux distribution pattern of a 300-nm-thick circular-shaped $YBa_2Cu_3O_{7-x}$ film after zero-field cooling and application of external magnetic fields $\mu_0 H_{ext}$ of (a) 24.6 mT, (b) 50.7 mT, (c) 76.4 mT, (d) 140.3 mT, (e) 187.4 mT perpendicular to the film and (f) in the remanent state after application of a maximum external field of 227.2 mT.

an unsymmetric current density and magnetic flux density distribution.

V. SUMMARY

By means of the magneto-optical Faraday effect, the magnetic flux density distribution was measured on the surface of a quadratic patterned superconducting $YBa_2Cu_3O_{7-x}$ thin film. The flux penetration takes place in several steps. The pattern observed after full flux penetration can be explained by a simple model. The currents flow parallel to the sample boarder in well-defined regions. These regions are separated by discontinuity planes where the current lines are discontinuous. This model can be applied to other geometries. For samples with homogeneous thickness and straight edges, an analytical $\mathbf{B}(\mathbf{r})$ solution can be given by superposition of the $\mathbf{B}(\mathbf{r})$ solution of cake like unit cells. For curved boundaries the $\mathbf{B}(\mathbf{r})$ distribution has to be computed numerically with modest effort. As an example, the $B_z(r)$ distribution of a cylindrical sample is presented.

The current has to adapt to macroscopic defects of the superconductor and flows around them, giving rise to a drastic change in the flux density distribution. These changes can also be calculated and are observed by the Faraday effect as funnel-like regions.

ACKNOWLEDGMENTS

The authors want to thank H.-U. Habermeier and B. Leibold from the technology group of the Max-Planck-Institut für Festkörperforschung for the preparation and patterning of the films.

[1] C. P. Bean, Phys. Rev. Lett. **8**, 250 (1962).
[2] E. H. Brandt, M. V. Indenbom, and A. Forkl, Europhys. Lett. **22**, 735 (1993).
[3] P. N. Mikheenko and Yu. E. Kuzovlev, Physica C **204**, 229 (1993).
[4] E. H. Brandt, Phys. Rev. Lett. **74**, 3025 (1995).
[5] Th. Schuster, H. Kuhn, and E. H. Brandt, Phys. Rev. B **50**, 16 684 (1994); Th. Schuster, M. V. Indenbom, H. Kuhn, M. Konczykowski, and E. H. Brandt, Phys. Rev. Lett **73**, 1424 (1994); Th. Schuster, H. Kuhn, and E. H. Brandt, Phys. Rev. B **51**, 697 (1995).
[6] B. J. Roth, N. G. Sepulveda, and J. P. Wikswo, Jr., J. Appl. Phys. **65**, 361 (1989).
[7] P. D. Grant, M. W. Denhoff, W. Xing, P. Brown, S. Govorkov, J. C. Irwin, B. Heinrich, H. Zhou, A. A. Fife, and A. R. Craig, Physica C **229**, 289 (1994); W. Xing, B. Heinrich, Hu Zhou, A. A. Fife, and A. R. Cragg, J. Appl. Phys. **76**, 4244 (1994).
[8] A. Forkl and H. Kronmüller, Physica C **228**, 1 (1994); A. Forkl, Phys. Scr. T **49**, 148 (1993).
[9] H. Theuss, A. Forkl, and H. Kronmüller, Physica C **190**, 345 (1992).
[10] F. M. Sauerzopf, H. P. Wiesinger, and H. W. Weber, Cryogenics **30**, 651 (1990).
[11] E. M. Gyorgy, R. B. van Dover, K. A. Jackson, L. F. Schneemeyer, and J. V. Wasczak, Appl. Phys. Lett. **55**, 283 (1994).
[12] A. Forkl, H.-U. Habermeier, B. Leibold, T. Dragon, and H. Kronmüller, Physica C **180**, 155 (1991).
[13] H.-U. Habermeier, Eur. J. Solid State Inorg. Chem. **28**, 619 (1991).
[14] V. A. Rowe, R. P. Huebener, and R. T. Kampwirth, Phys. Status Solidi A **4**, 513 (1971).
[15] P. Brüll, D. Kirchgässner, and P. Leiderer, Physica C **182**, 339 (1991).
[16] Th. Schuster, M. Leghissa, M. R. Koblischka, H. Kuhn, M. Kraus, H. Kronmüller, and G. Saemann-Ischenko, Physica C **203**, 203 (1992).
[17] V. K. Vlasko-Vlasov, M. V. Indenbom, V. I. Nikitenko, A. A. Polyanskii, R. L. Prozorov, I. V. Grekhov, L. A. Delimova, I. A. Liniichuk, A. V. Antonov, and M. Yu. Gusev, Superconductivity **5**, 1582 (1992).
[18] A. M. Campbell and J. E. Evetts, Adv. Phys. **72**, 199 (1972).

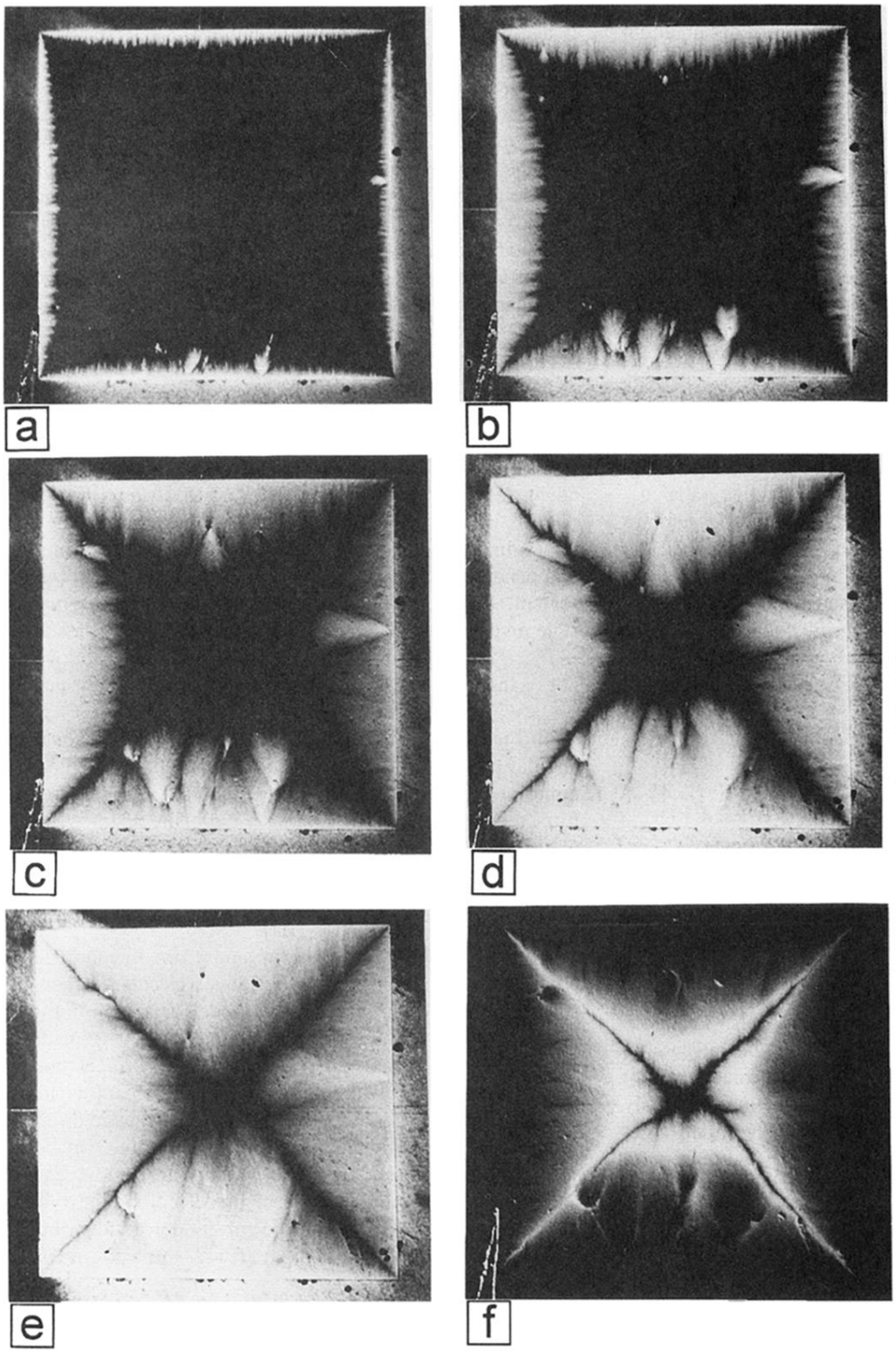

FIG. 1. Magnetic flux distribution pattern of a 300-nm-thick square-shaped $YBa_2Cu_3O_{7-x}$ film after zero-field cooling and application of external magnetic fields $\mu_0 H_{ext}$ of (a) 26.5 mT, (b) 44.3 mT, (c) 73.2 mT, (d) 100.3 mT, (e) 155.5 mT perpendicular to the film and (f) in the remanent state.

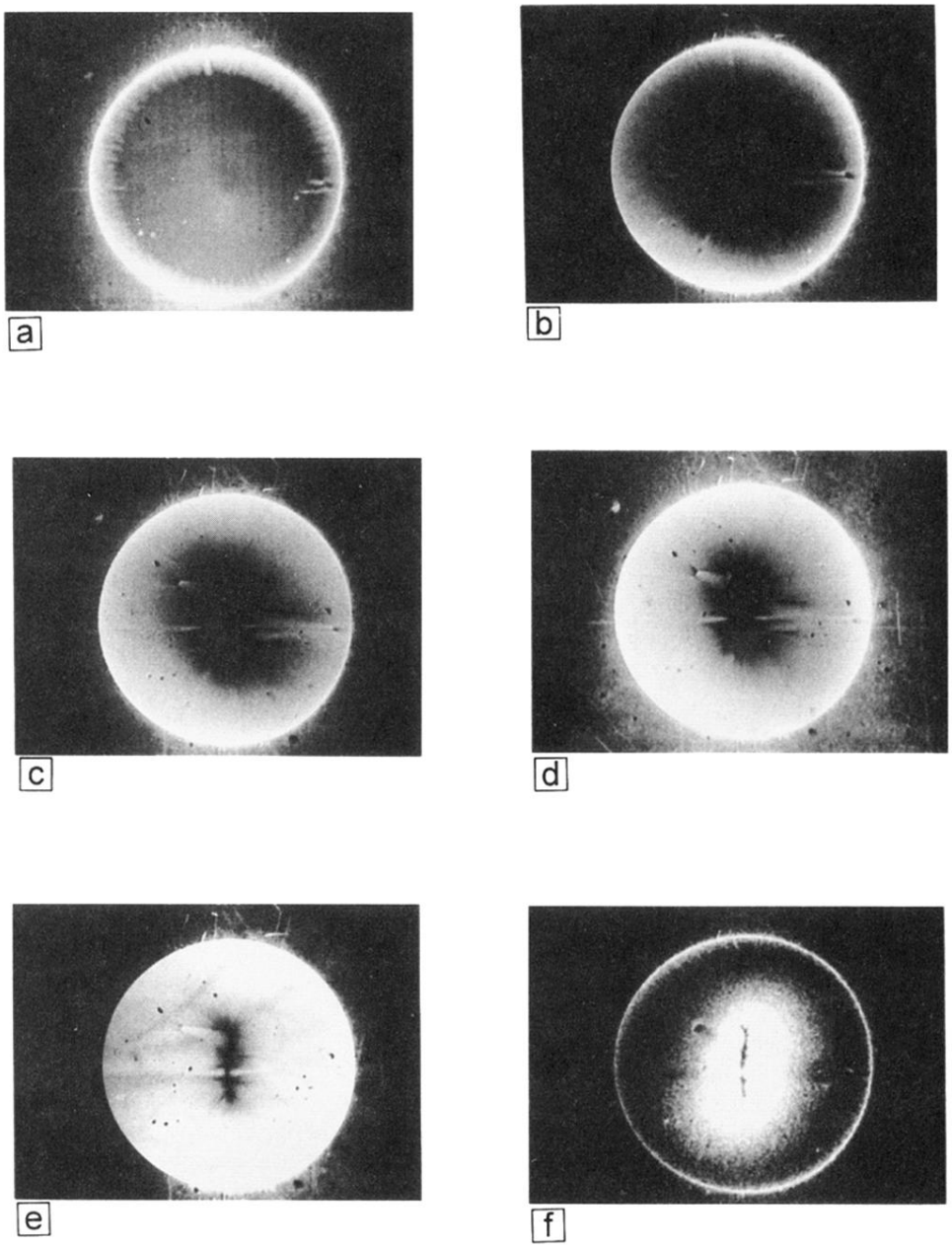

FIG. 11. Magnetic flux distribution pattern of a 300-nm-thick circular-shaped $YBa_2Cu_3O_{7-x}$ film after zero-field cooling and application of external magnetic fields $\mu_0 H_{ext}$ of (a) 24.6 mT, (b) 50.7 mT, (c) 76.4 mT, (d) 140.3 mT, (e) 187.4 mT perpendicular to the film and (f) in the remanent state after application of a maximum external field of 227.2 mT.

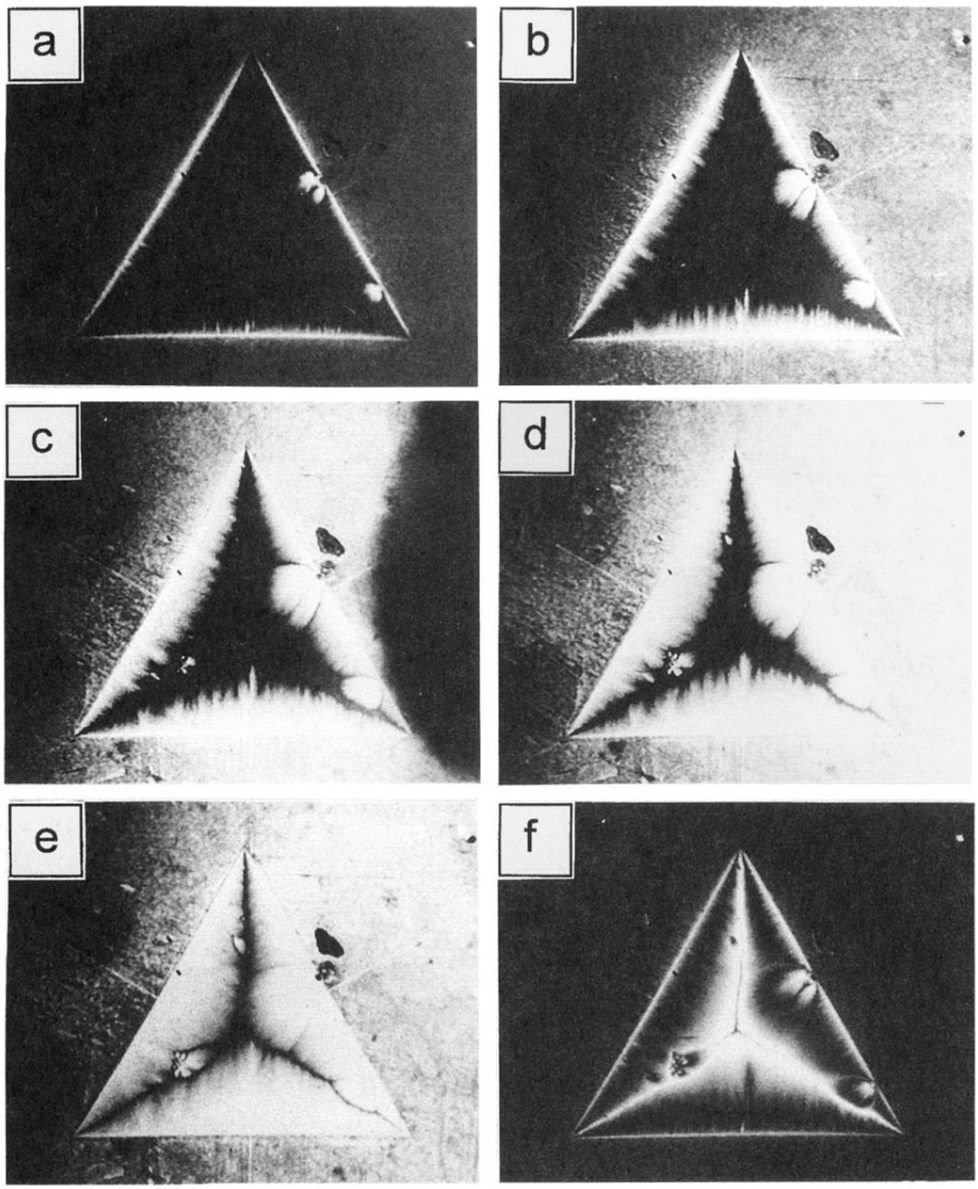

FIG. 2. Magnetic flux distribution pattern of a 300-nm-thick triangular-shaped $YBa_2Cu_3O_{7-x}$ film after zero-field cooling and application of external magnetic fields $\mu_0 H_{ext}$ of (a) 19.5 mT, (b) 38.0 mT, (c) 56.3 mT, (d) 75.4 mT, (e) 135.3 mT perpendicular to the film and (f) in the remanent state after application of a maximum external field of 222.3 mT.

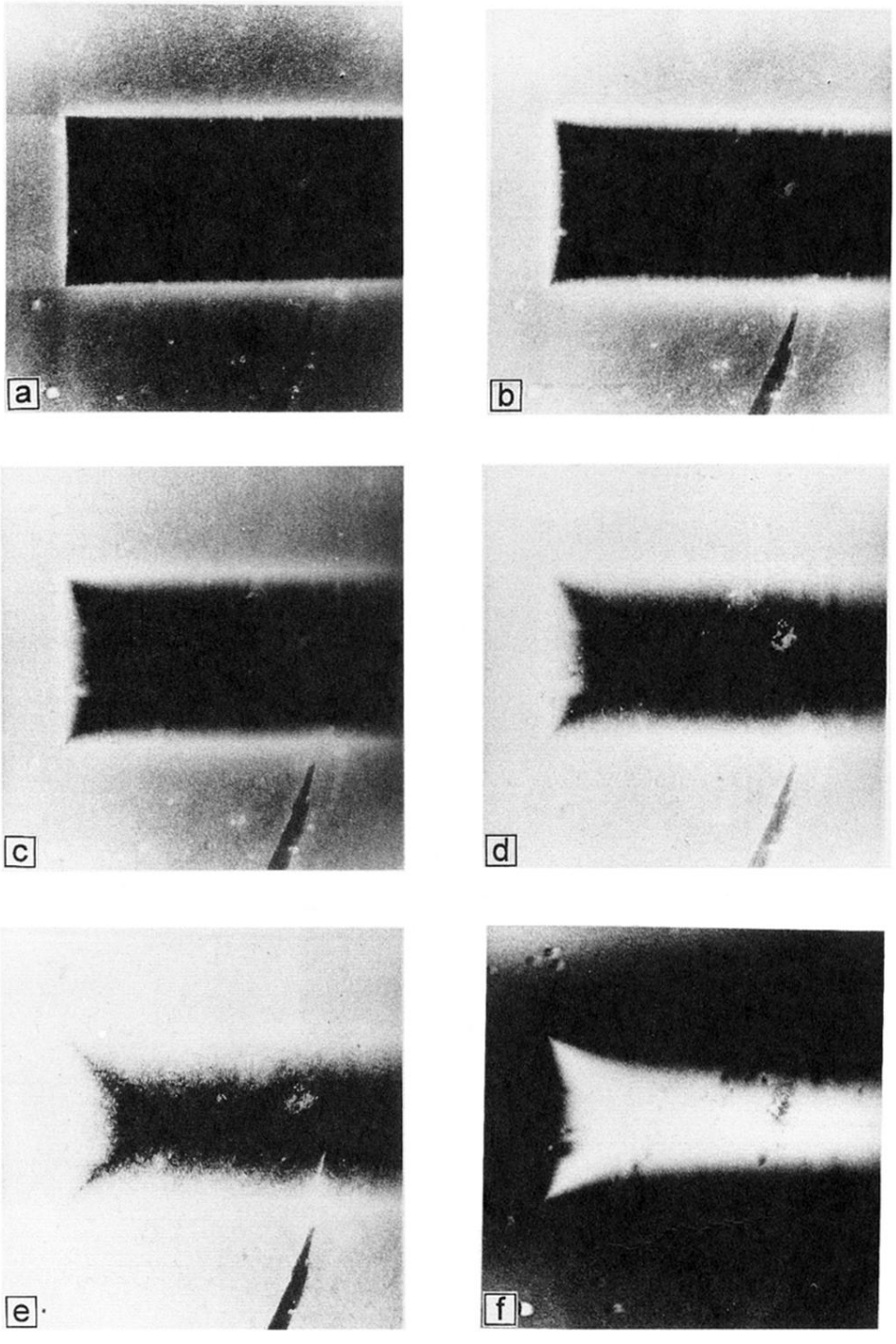

FIG. 3. Magnetic flux distribution pattern of a 300-nm-thick rectangular-shaped $YBa_2Cu_3O_{7-x}$ film after zero-field cooling and application of external magnetic fields $\mu_0 H_{ext}$ of (a) 32.9 mT, (b) 65.8 mT, (c) 98.7 mT, (d) 131.6 mT, (e) 197.4 mT perpendicular to the film and (f) in the remanent state after application of a maximum external field of 263.5 mT.

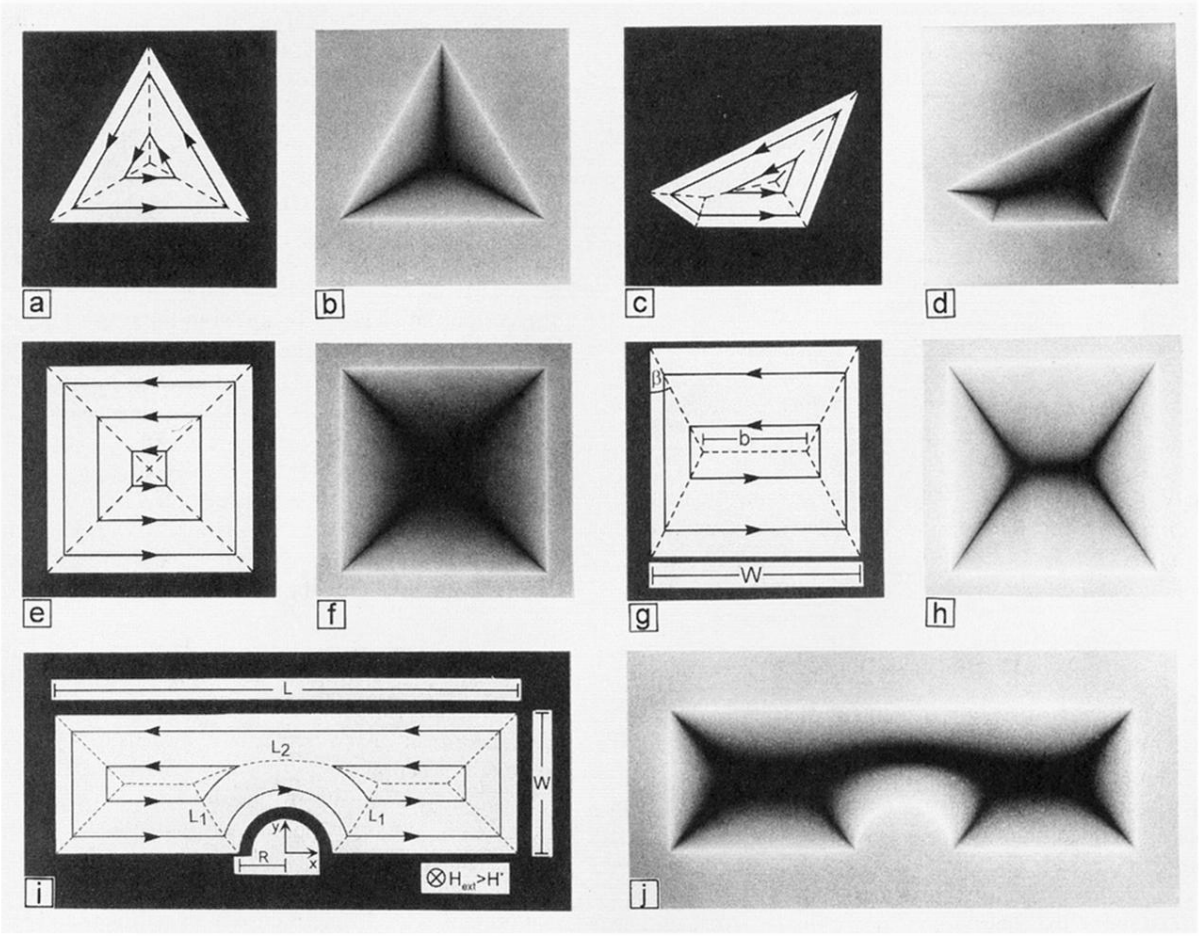

FIG. 6. Current paths and calculated distribution of the B_z component of the magnetic flux density distribution for different sample geometries. Dashed lines belong to the cut of the discontinuity planes with the xy plane; i.e., here the currents change direction. The external magnetic field is always applied perpendicular to the observation plane. (a) and (b) Triangular sample, (c) and (d) irregular polygon-shaped sample, (e) and (f) quadratic sample with anisotropy factor $A=1.0$, (g) and (h) quadratic sample with anisotropic current, i.e., parallel to the horizontal edge flows a lower current $j_{cl}=0.5j_{ch}$ than parallel to the vertical edge (j_{ch}), (i) and (j) rectangular sample with semicircular defect at the edge (radius R). For details see the text.

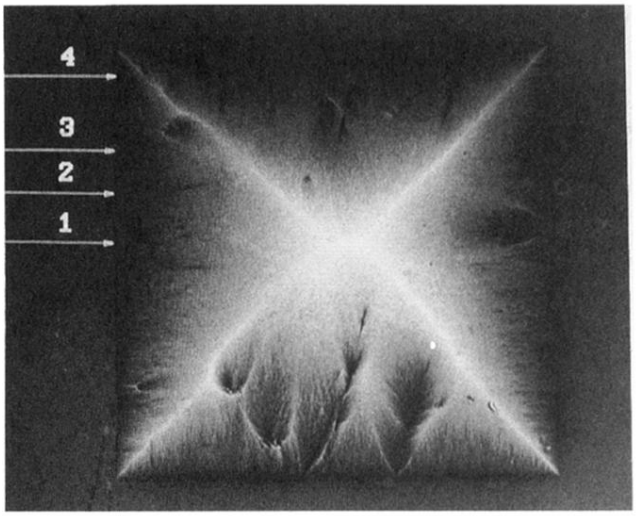

FIG. 9. Remanent magnetic flux distribution pattern of the film shown in Figs. 1(a)–1(f) after application of an external field $\mu_0 H_{ext}$ of 400 mT and reducing to zero.